METALLOENZYMES

Structures of the nitrogenase complex prepared under catalytic turnover conditions

Hannah L. Rutledge, Brian D. Cook, Hoang P. M. Nguyen, Mark A. Herzik Jr.*, F. Akif Tezcan*

The enzyme nitrogenase couples adenosine triphosphate (ATP) hydrolysis to the multielectron reduction of atmospheric dinitrogen into ammonia. Despite extensive research, the mechanistic details of ATP-dependent energy transduction and dinitrogen reduction by nitrogenase are not well understood, requiring new strategies to monitor its structural dynamics during catalytic action. Here, we report cryo–electron microscopy structures of the nitrogenase complex prepared under enzymatic turnover conditions. We observe that asymmetry governs all aspects of the nitrogenase mechanism, including ATP hydrolysis, protein-protein interactions, and catalysis. Conformational changes near the catalytic iron-molybdenum cofactor are correlated with the nucleotide-hydrolysis state of the enzyme.

Reduced forms of nitrogen are essential for the biosynthesis of amino acids and nucleic acids as well as the production of fertilizers and many commodity chemicals (*1*). As the only enzyme capable of nitrogen fixation, nitrogenase catalyzes the eight-electron reduction of atmospheric nitrogen (N_2) and protons (H^+) into ammonia (NH_3) and hydrogen (H_2) (*2*, *3*) (Fig. 1A). Nitrogenase is a two-component enzyme, which, in its most common form, consists of the iron protein FeP (a γ_2 homodimer) and the molybdenum-iron protein MoFeP (an $\alpha_2\beta_2$ heterotetramer) (Fig. 1B) (*4*, *5*). Nitrogenase is distinct from most redox enzymes in its requirement for adenosine triphosphate (ATP) hydrolysis to enable the successive transfer of electrons and protons for substrate reduction (*6*, *7*). The coupling of ATP hydrolysis to electron transfer (ET) is mediated by FeP, which forms a specific, nucleotide-dependent complex with MoFeP and hydrolyzes two ATP molecules for the transfer of an electron to MoFeP (*4*–*7*). This part of nitrogenase catalysis is termed the FeP cycle (Fig. 1A) (*2*, *8*). In the MoFeP cycle (Fig. 1A) (*2*, *8*), the electrons from FeP are received by the P-cluster (an [8Fe:7S] complex) of MoFeP and relayed to the iron-molybdenum cofactor FeMoco (a [7Fe:9S:C:Mo]-homocitrate complex), where N_2 binding and reduction occur. Specific ATP-dependent interactions between FeP and MoFeP are necessary not only for interprotein ET but also for gated ET between the P-cluster and FeMoco through long-distance conformational perturbations, the nature of which are not understood (*6*, *7*).

Although the dynamic coupling between ATP hydrolysis and ET ultimately drives N_2 fixation, it also creates experimental challenges for a mechanistic understanding of

Department of Chemistry and Biochemistry, University of California, San Diego, La Jolla, CA 92093, USA.
*Corresponding author. Email: tezcan@ucsd.edu (F.A.T.); mherzik@ucsd.edu (M.A.H.)

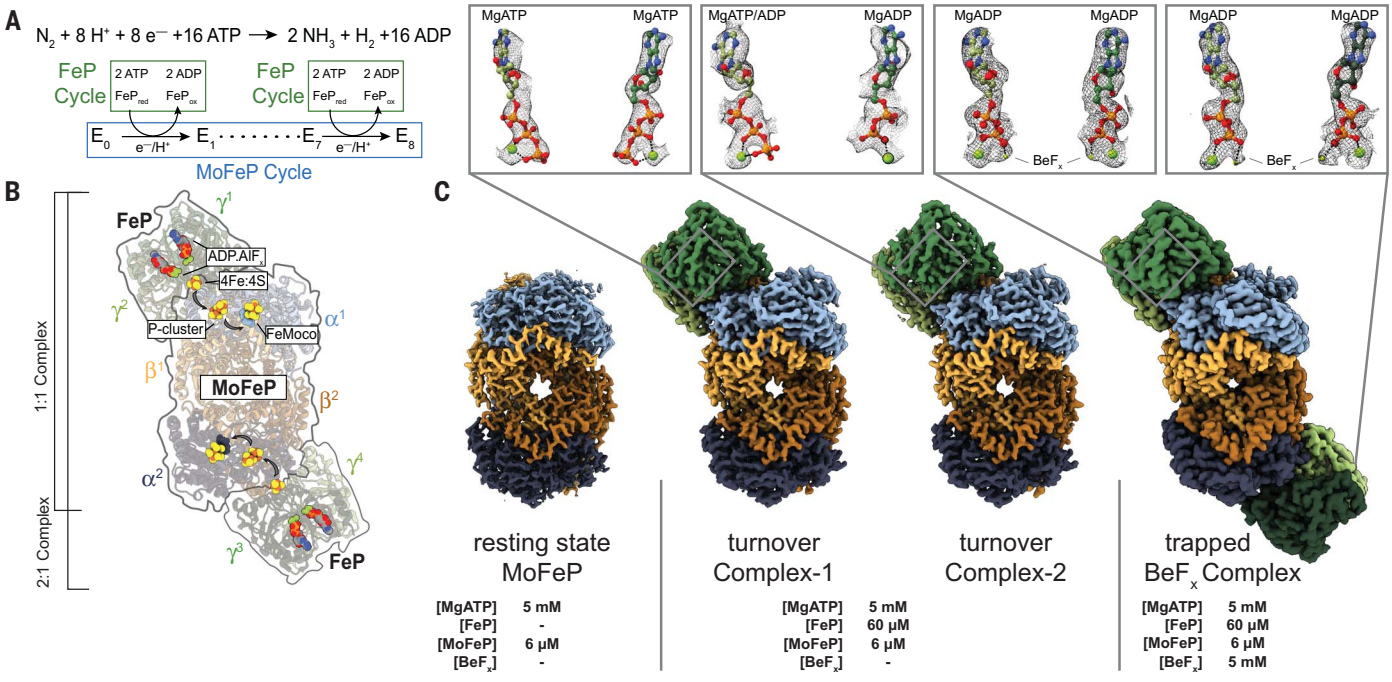

Fig. 1. Catalytic cycle for nitrogenase and its structural characterization under nonturnover and turnover conditions. (**A**) Chemical reaction catalyzed by nitrogenase. There are eight FeP cycles in each MoFeP cycle. (**B**) Crystal structure (PDB ID 1M34) (*10*) of the 2:1 FeP:MoFeP complex stabilized by MgADP.AlF_x, showing the relative positions of the individual FeP (γ^1 to γ^4) and MoFeP ($\alpha^1\beta^1\alpha^2\beta^2$) subunits, the nucleotides, and the metalloclusters. The FeP subunits are shown in dark green (γ^1 or γ^3) and light green (γ^2 or γ^4), and the MoFeP subunits are highlighted in light blue (α^1), dark blue (α^2), light orange (β^1), and dark orange (β^2). Black arrows indicate the path of electron flow. (**C**) Cryo-EM maps of ^{rs}MoFeP (~1.8-Å resolution) obtained in the absence of FeP; $^{t/o}$Complex-1 (~2.3-Å resolution) and $^{t/o}$Complex-2 (~2.3-Å resolution) obtained under turnover conditions; and the BeF_x-trapped FeP-MoFeP complex (~2.4-Å resolution). Coloring scheme for the subunits is the same as in (B). Cryo-EM maps for nucleotides are shown as a gray mesh and contoured at the following levels: ^{rs}MoFeP, 0.008; $^{t/o}$Complex-1, 0.17; and $^{t/o}$Complex-2, 0.075. Magnified views of the nucleotides bound to the nitrogenase complexes and their corresponding cryo-EM densities are shown in boxes.

nitrogenase. First, substrates and inhibitors can only bind reduced forms of FeMoco, whose generation requires continuous turnover conditions that include ATP and reduced FeP (*2*, *3*). Because MoFeP is also an inherent hydrogenase, such reduced forms of FeMoco promptly return to the resting state through H_2 evolution upon termination of ATP hydrolysis (*8*, *9*), rendering substrate-bound states of FeMoco too fleeting for structural characterization. Second, the necessity of continuous ATP hydrolysis for catalysis leads to a heterogeneous distribution of nitrogenase substates that are difficult to interrogate experimentally. These substates differ not only in the FeP-MoFeP complexation state and the extent of ATP hydrolysis within the FeP cycle but also in the oxidation states of the metal cofactors and the reaction intermediates on FeMoco (E_0 to E_8) within the MoFeP cycle (Fig. 1, A and B).

Previous crystallographic studies have provided detailed views of the nucleotide-dependent conformations of the FeP-MoFeP complexes and outlined the path of ET in nitrogenase (Fig. 1B) (*10*, *11*). Yet, these static views, which were obtained under nonturnover conditions and constrained by crystal lattice, showed no variation in the structure of MoFeP, providing little insight into the mechanism of ATP/FeP-mediated redox events within this protein. Recent crystallographic studies of MoFeP and its vanadium analog, VFe-protein, revealed possible modes of ligand interactions with FeMoco and showed that the cofactor is capable of undergoing compositional changes (*12*–*14*). However, these structural snapshots were obtained using crystals that formed hours to days after the last enzymatic turnover reaction, and their catalytic relevance remains an open question. In parallel, extensive freeze-quench spectroscopic studies of nitrogenase have characterized substrate- and intermediate-bound states of FeMoco (*15*, *16*). Yet, these methods do not report on the atomic structure of the cofactor as a whole and provide little information regarding how the local cofactor-ligand interactions are linked to global ATP/FeP-dependent structural dynamics of MoFeP. Consequently, we lack a detailed understanding of why and how ATP hydrolysis is used to drive N_2 fixation and how catalysis at FeMoco proceeds. Clearly, new experimental approaches are needed to structurally interrogate nitrogenase during catalysis at or near atomic resolution to simultaneously characterize the ATP-dependent FeP-MoFeP interactions and the associated structural dynamics within each protein.

We sought to overcome some limitations of prior studies by using cryo–electron microscopy (cryo-EM) to directly visualize nitrogenase under enzymatic turnover conditions. We prepared cryo-EM samples of *Azotobacter vinelandii* nitrogenase under high-electron flux turnover conditions (see supplementary methods), which contained a 10-fold molar excess of FeP over MoFeP and low ionic strength (≤25 mM NaCl) to favor the formation of electrostatically driven FeP-MoFeP complexes. We included sufficient MgATP and dithionite (5 mM each) to ensure that they are not depleted during turnover while minimizing background electron scattering. Turnover samples were prepared anaerobically under a N_2 atmosphere in an anaerobic glovebox and flash frozen in liquid N_2 within 15 s after initiation of turnover. For purposes of rapid manual freezing of cryo-EM grids, these turnover samples were removed from the glovebox, thawed, applied to grids, blotted, and frozen within <15 s. The ~30-s total preparation period was sufficiently long to ensure that steady-state catalytic conditions were reached but short enough such that there was still remaining reductant and MgATP in solution (see supplementary methods). We collected a large cryo-EM dataset (>15,000 movies) that yielded >4.5 million usable particles (figs. S1 and S2 and table S1). Through exhaustive two-dimensional (2D) and 3D classification and refinement, we isolated free MoFeP (~60%) and FeP particles (~5%), as well as FeP-MoFeP nitrogenase assemblies (~35%), from this heterogeneous mixture. We determined the structures of two conformationally distinct 1:1 FeP:MoFeP complexes under turnover conditions, designated $^{t/o}$Complex-1 and $^{t/o}$Complex-2, at ~2.3-Å resolution (Fig. 1C). Both complexes contain intact FeP and reduced, all-ferrous P-clusters (vide infra), indicating the lack of potential oxidation or damage by O_2 to the clusters. As a reference, we also obtained a ~1.8-Å resolution cryo-EM structure of resting-state MoFeP, termed ^{rs}MoFeP, using the same turnover conditions but in the absence of FeP (Fig. 1C, fig. S3, and table S2).

Given the C_2 symmetry of MoFeP and the large separation (>65 Å) between the nearest clusters from the symmetry-related αβ subunits, it has long been assumed that the two αβ halves of MoFeP function independently from one another (*2*, *8*). In support of this assumption, the crystal structures of various FeP-MoFeP complexes in different nucleotide-bound states largely possess a 2:1 FeP:MoFeP stoichiometry (Fig. 1B) (*10*, *11*, *17*). Unexpectedly, our turnover samples did not contain any particles that could be assigned to a 2:1 FeP:MoFeP complex (Fig. 1C and fig. S1). We considered the possibility that the exclusive observation of 1:1 complexes in our turnover samples could arise from an experimental artifact such as protein degradation or an increase in ionic strength during cryo-EM grid preparation. Therefore, we prepared a second set of turnover samples in the same manner as above that also included 5 mM beryllium fluoride (BeF_x), which is known to arrest ATP hydrolysis in a transition-like state to yield quasi-irreversible, solution-stable 2:1 and 1:1 FeP-MoFeP complexes (*18*). Accordingly, our cryo-EM samples contained a large fraction of 2:1 FeP:MoFeP complexes alongside 1:1 species but no detectable free MoFeP particles (figs. S4 and S5 and table S3). We determined the structure of the MgADP.BeF_x-bound 2:1 FeP:MoFeP at ~2.4-Å resolution and found it to be isostructural to the crystal structure of the related MgADP.AlF_x-bound 2:1 FeP:MoFeP complex [Protein Data Bank (PDB) ID 1M34; Fig. 1C and fig. S5]. These observations affirm that our cryo-EM samples contain intact proteins and operate under native turnover conditions, in turn indicating that the 1:1 FeP:MoFeP stoichiometry is the predominant nitrogenase assembly state during catalysis.

Prior work using pre–steady-state kinetics measurements revealed that the extents of interprotein ET and ATP hydrolysis were approximately half of what would be expected if there were two independent FeP binding sites on MoFeP (*19*). Originally, such half-reactivity was attributed to either partial inactivity of FeP molecules (*19*) or to the possible existence of an alternative interaction mode between FeP and MoFeP (*20*). Recent studies favored a model of negative cooperativity within a 2:1 FeP:MoFeP complex, whereby one of the bound FeP molecules suppresses ATP hydrolysis by the other bound FeP and the redox activity of the opposite αβ half of MoFeP (*21*, *22*). Our cryo-EM structures instead suggest that half-reactivity and negative cooperativity in nitrogenase arise from MoFeP binding to only one FeP molecule at a time during turnover.

$^{t/o}$Complex-1 and $^{t/o}$Complex-2 were distinguished during cryo-EM data processing primarily on the basis of the structural variability of the FeP components. Thus, we first examined whether these differences are associated with the ATP-hydrolysis state of the two complexes. Earlier crystal structures identified at least three nucleotide state–dependent FeP-MoFeP docking geometries (DG1 to DG3) and led to the hypothesis that FeP moves in a unidirectional fashion across the MoFeP surface during turnover (Fig. 2A) (*6*, *11*). The DG1 state predominates in the absence of nucleotides but is also populated in the presence of ATP (*23*) and corresponds to an electrostatically guided encounter complex wherein FeP largely interacts with the β subunit of MoFeP. DG2 is the activated nitrogenase complex in which ATP hydrolysis is coupled to interprotein ET, with FeP occupying the quasi-symmetric surface of MoFeP shared between α and β subunits (Figs. 1B and 2A) (*10*, *11*). Finally, DG3 is formed by adenosine diphosphate (ADP)–bound FeP and primarily uses the α-subunit surface of MoFeP (*11*). The cryo-EM analysis of our

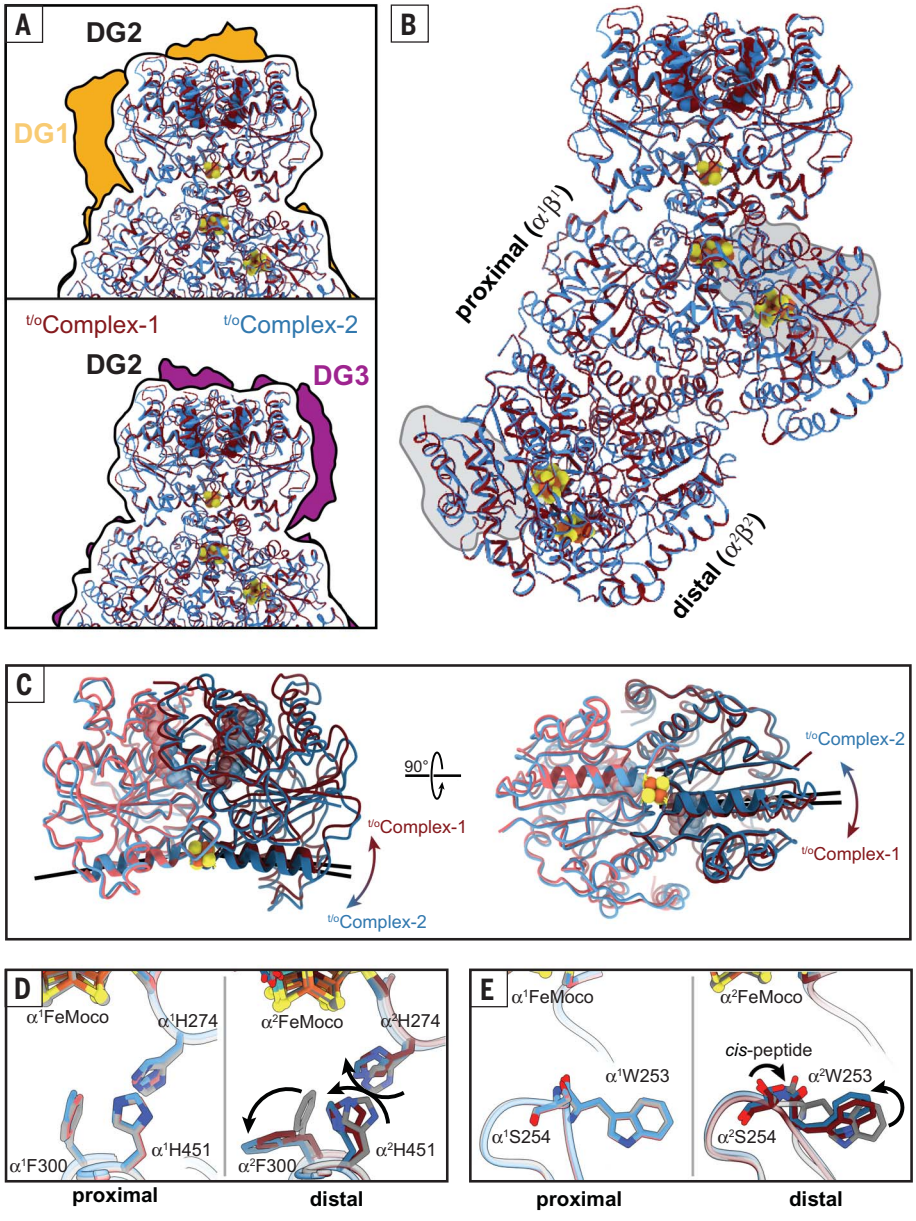

Fig. 2. Structural details of nitrogenase complexes characterized under turnover conditions. (**A**) The FeP:MoFeP docking geometry (DG) in $^{t/o}$Complex-1 (maroon) and $^{t/o}$Complex-2 (blue) observed in the DG2 configuration (black outline) compared with the DG1 (gold; PDB ID 2AFH) and DG3 (purple; PDB ID 2AFI) configurations characterized by x-ray crystallography (*11*). (**B**) Structural overlay of $^{t/o}$Complex-1 and $^{t/o}$Complex-2, indicating that the only large-scale conformational changes are observed in FeP. "Proximal" and "distal" refer to the $\alpha^1\beta^1$ and $\alpha^2\beta^2$ halves of MoFeP bound and not bound to FeP, respectively. The αIII domains of MoFeP are outlined in gray. (**C**) Structural overlay of the FeP components in $^{t/o}$Complex-1 and $^{t/o}$Complex-2, highlighting the nucleotide-dependent conformational differences [hinging (left) and twisting (right)] motions of the γ^1 and γ^2 subunits relative to one another during ATP hydrolysis. The axes of the γ100's helices (residues γ98 to γ112) that radiate from the [4Fe:4S] cluster are shown as black lines to illustrate these conformational differences. (**D** and **E**) Residues in the vicinity of FeMoco [(D) αHis^{274}, αPhe^{300}, and αHis^{451}; (E) αTrp^{253}] that have undergone conformational changes in the distal subunit (α^2) of MoFeP during turnover. Movements between the resting-state (^{rs}MoFeP) (gray) and the turnover structures (maroon and blue) are indicated with arrows. F, Phe; H, His; S, Ser; W, Trp.

turnover samples revealed that $^{t/o}$Complex-1 and $^{t/o}$Complex-2 were exclusively in DG2 (Fig. 2A), implying that this configuration has a higher stability and/or longer residence time relative to DG1 and DG3. Characteristic of a DG2 configuration, both complexes feature extensive interactions between FeP and MoFeP (buried surface areas >3600 Å^2) and a short [4Fe:4S]-to-P-cluster edge-to-edge distance of ~15 Å, primed for rapid interprotein ET (Fig. 2B). In $^{t/o}$Complex-1, both FeP γ subunits (γ^1 and γ^2) are occupied by ATP molecules with clear densities for the γ-phosphate groups and associated Mg^{2+} ions (Fig. 1C). By contrast, the γ^1 subunit of $^{t/o}$Complex-2 features an ATP molecule with weak density for the γ-phosphate, whereas the γ^2 subunit is ADP-bound and the γ-phosphate is completely absent from the nucleotide binding pocket, indicative of asymmetry in ATP hydrolysis (Fig. 1C). This observation is consistent with the crystal structure of a mixed-nucleotide FeP-MoFeP complex, in which AMPPCP (a nonhydrolyzable ATP analog) and ADP were selectively bound to the γ^1 and γ^2 subunits, respectively (*24*). The differences in the nucleotide occupancies of $^{t/o}$Complex-1 and $^{t/o}$Complex-2 are reflected in their distinct FeP conformations (Fig. 2C), which is further corroborated by a principal components analysis of available FeP structures (fig. S6). Collectively, we infer that (i) our cryo-EM structures report on active turnover states from the standpoint of ATP hydrolysis by FeP, (ii) the hydrolysis of two ATP molecules in each FeP cycle occurs in a stepwise fashion, and (iii) $^{t/o}$Complex-1 and $^{t/o}$Complex-2 correspond, respectively, to pre- and mid–ATP hydrolysis states of the nitrogenase complex that are populated along the catalytic reaction coordinate.

The asymmetry present both in ATP hydrolysis and FeP-MoFeP interactions has important implications for the timing of ET events during catalysis. Compared with a concerted process, stepwise nucleotide hydrolysis by FeP would be expected to increase the lifetime of the activated DG2 complex and provide additional conformational states for orchestrating the multistep redox reactions that occur at FeMoco and the P-cluster (*6*, *24*). Similarly, an alternating docking mechanism between FeP and MoFeP (as imposed by negative cooperativity between the αβ halves) would effectively slow down successive ET steps to a given αβ subunit, providing sufficient time for anticipated protein and metallocluster rearrangements during N_2 reduction. This is consistent with the suggestion of Thorneley and Lowe that the slow kinetics of nitrogenase [turnover rate ($k_{turnover}$) ≈ 1 s^{-1}] governed by FeP-MoFeP interactions may be a mechanistic imperative to favor N_2 fixation over the competing but less demanding H^+ reduction (*8*).

Having analyzed $^{t/o}$Complex-1 and $^{t/o}$Complex-2 in the context of the FeP cycle, we next investigated whether they exhibited any conformational changes in their MoFeP components that may be correlated with the ATP hydrolysis state. In both $^{t/o}$Complex-1 and $^{t/o}$Complex-2, the P-clusters are in their fully reduced, all-ferrous (P^N) forms (fig. S7), and the protein

backbone arrangements of MoFeP's in both complexes are essentially indistinguishable from one another as well as from those in ^{rs}MoFeP and previously determined MoFeP crystal structures (Cα root mean square deviation of 0.2 Å; Fig. 2B, fig. S8, and table S4). We observed no large-scale conformational changes that could account for mechanical coupling and negative cooperativity between symmetry-related FeP docking surfaces on MoFeP, implicating the involvement of a dynamic allosteric mechanism (e.g., FeP-induced changes in MoFeP conformational entropy) (fig. S9) (*25*). Yet, a detailed inspection of the structures revealed that the FeP-free (i.e., "distal") $\alpha^2\beta^2$ half in both $^{t/o}$Complex-1 and $^{t/o}$Complex-2 possessed several features that distinguish it from the FeP-bound (i.e., "proximal") $\alpha^1\beta^1$ half and ^{rs}MoFeP.

First, there are several conserved residues (α^2Trp^{253}, α^2His^{274}, α^2Phe^{300}, α^2His^{451}) (*26*) in the vicinity of the distal FeMoco that adopt non–resting state conformations (Fig. 2, D and E). αTrp^{253} is particular in its *cis* peptide bond to αSer^{254} and its position in a proposed substrate access channel from the protein surface to FeMoco (*27*, *28*). The observed conformational flip in α^2Trp^{253} leads to the diversion of this putative channel to an alternate face of FeMoco (Fig. 2E and fig. S10). α^2His^{274}, α^2Phe^{300}, and α^2His^{451} side chains appear to have undergone a concerted motion compared with their resting state (Fig. 2D), whereby α^2His^{274} and α^2Phe^{300} assume a similar configuration as that seen in the low-pH crystal structure of MoFeP (fig. S11) (*29*). This αHis^{274} configuration was proposed to form a water-bridged H bond to a protonated belt sulfur (S5A) of FeMoco (*29*). Along these lines, the observed rearrangement of the α^2His^{274} side chain in the turnover complexes could be envisioned to stabilize a protonated FeMoco intermediate and/or to increase the reduction potential of the cofactor, thus promoting its reduction by the P-cluster.

Second, the cryo-EM densities surrounding the α^2His^{442} and homocitrate ligands to the Mo center of the distal FeMoco are considerably less well defined compared with their counterparts in the proximal αβ half and the residues in the vicinity (fig. S12) and cannot be modeled with the resting-state configurations of these ligands (Fig. 3). The reduction in map density is particularly pronounced for $^{t/o}$Complex-2 (i.e., mid–ATP hydrolysis) compared with that of $^{t/o}$Complex-1 (i.e., pre–ATP hydrolysis). These observations suggest that α^2His^{442} and homocitrate are mobile during turnover and that Mo undergoes changes in innersphere coordination in a way that is correlated with the nucleotide hydrolysis state of FeP bound to the opposing αβ half of MoFeP. The substitution of Mo with V or Fe in alternative nitrogenases, the replacement of homocitrate with citrate, and alterations in H bonding to homocitrate have been shown to substantially diminish N_2 reduction activity and alter substrate specificity (*2*, *30*–*32*). Indeed, the direct involvement of the Mo center in N_2 reduction has been proposed early on (*2*, *33*), although recent experimental findings have shifted the focus to the central Fe centers of FeMoco as being the primary sites for substrate activation (*15*, *16*). Our cryo-EM observations provide evidence that the Mo-homocitrate moiety may also participate in dynamic structural transformations that accompany catalysis at FeMoco.

Third, portions of a large domain in the distal αβ subunit comprising residues α25 to α48 and α378 to α403 (particularly in $^{t/o}$Complex-2) possess increased mobility compared with the rest of the MoFeP (fig. S13). This so-called αIII domain forms a lid above FeMoco and includes residues αGlu^{380} and αPhe^{381}, which form close contacts with FeMoco (Figs. 2B and 3). In resting-state MoFeP, αIII is well ordered, αGlu^{380} forms water-bridged H bonds to the Mo-ligated αHis^{442} side chain and homocitrate, and αPhe^{381} is in van der Waals contact with the labile belt sulfide S2B of FeMoco (Fig. 3A). By contrast, in the distal αβ halves of $^{t/o}$Complex-1 and $^{t/o}$Complex-2, the cryo-EM densities for αIII and the side chains of α^2Glu^{380} and α^2Phe^{381} are either diffuse or entirely missing (Fig. 3B and fig. S13). This movement is likely coupled to the dynamics of the Mo ligands and FeMoco as a whole. αIII has also been shown to undergo major structural rearrangements associated with the insertion of FeMoco into MoFeP (*34*). Furthermore, αIII displays some of the highest temperature factors in MoFeP crystal structures and is positioned away from lattice contacts (table S5)

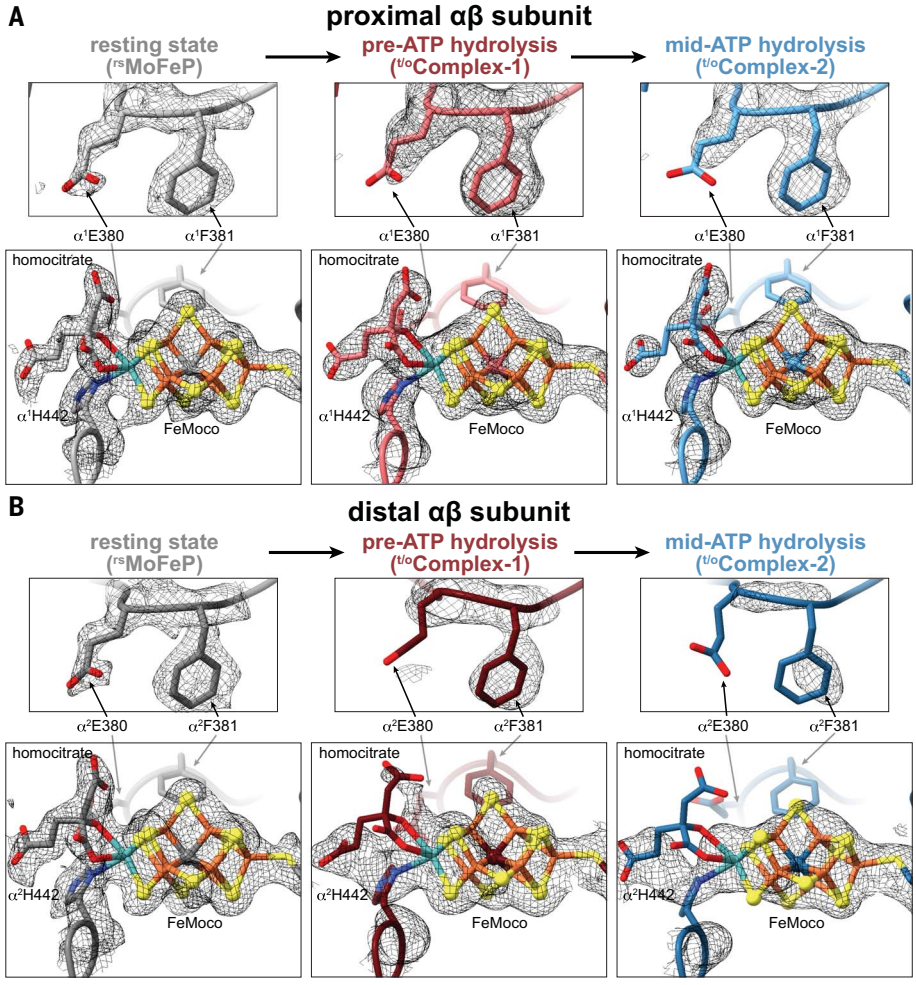

Fig. 3. Changes in the FeMoco environment observed during catalytic turnover. (**A** and **B**) Views of FeMoco and the nearby residues αGlu^{380} and αPhe^{381} in the proximal (A) and distal (B) αβ halves of MoFeP in ^{rs}MoFeP (gray), $^{t/o}$Complex-1 (maroon), and $^{t/o}$Complex-2 (blue) structures. Cryo-EM maps for each individual structure are shown as a gray mesh and contoured at the following levels: ^{rs}MoFeP, 0.008; $^{t/o}$Complex-1, 0.065; and $^{t/o}$Complex-2, 0.075. E, Glu.

(*10*, *11*, *24*, *29*, *35*), implying that it is inherently more flexible than other parts of MoFeP. Combined with this observation, $^{t/o}$Complex-1 and $^{t/o}$Complex-2 structures point to a possible role of αIII mobility in nitrogenase catalysis. Notably, αIII abuts the docking surface of MoFeP for MgADP-bound FeP in DG3 and may lie in the trajectory of FeP moving directionally across the MoFeP surface during ATP hydrolysis (*11*). Thus, a dynamic αIII domain could also provide a direct mechanical conduit between FeP and the proximal FeMoco, further linking the timing of nucleotide-dependent FeP-MoFeP interactions to redox transformations at FeMoco. The increased mobility of the αIII domain and the lack of a capping FeP could also allow more efficient substrate or molecular access to or exit from FeMoco.

Based on the available structures, it is not obvious (i) how FeP docking induces conformational changes in the distal αβ subunit of MoFeP over a distance of ≥80 Å or (ii) to which states of the MoFeP cycle (i.e., E_0 to E_8) the observed nitrogenase complexes correspond. It is safe to assume, however, that all copies of FeMoco in these complexes represent the more stable or longer-lived of the many catalytic intermediates present in the turnover solution. The density maps for the proximal FeMoco's are essentially identical to those for the resting-state cofactor (Fig. 3). Thus, an assignment of E_0 for the proximal cofactors is plausible, although E_1 to E_4 are also reasonable because these states have been proposed as hydride-bound FeMoco intermediates (*15*, *16*), which may be structurally indistinguishable from E_0 at the current resolution of these cryo-EM maps. At the same time, the obvious deviations between the densities of distal and proximal FeMoco's indicate that the distal cofactors in $^{t/o}$Complex-1 and $^{t/o}$Complex-2 might represent an E_x state or a mixture of E_x states that are different from the proximal cofactors and previous crystal structures solved in the resting state of FeMoco. It is thus possible that this structure represents a more advanced state in the MoFeP cycle (i.e., ≥E_1) than the proximal FeMoco's and involves the participation of the Mo center. We also note that the overall map density for the distal FeMoco in $^{t/o}$Complex-2 is less well defined than in those in ^{rs}MoFeP, $^{t/o}$Complex-1, or the proximal subunit in $^{t/o}$Complex-2, which may further indicate conformational changes in the cofactor during turnover such as the displacement of belt sulfurs or ligand binding (*12*–*14*). Given the asymmetry between the FeMoco's in the two αβ halves, it is tempting to propose a "ping-pong"–type mechanism in which the cofactors proceed through each of the eight catalytic steps in an alternating fashion. This scenario would assign a dual role to FeP: (i) to deliver an electron to one αβ subunit of MoFeP and (ii) to suppress FeP binding to the opposite αβ subunit while priming it for catalytic transformations through long-distance activation of electron, H^+, and/or substrate access pathways to the distal FeMoco. Establishing whether such a mechanism is operative will require future studies, but our current work illustrates that it is possible to characterize nitrogenase under turnover conditions by cryo-EM at near-atomic resolution, representing a critical step toward understanding the mechanism of this enigmatic enzyme in full structural detail.

REFERENCES AND NOTES

1. V. Smil, *Sci. Am.* **277**, 76–81 (1997).
2. B. K. Burgess, D. J. Lowe, *Chem. Rev.* **96**, 2983–3012 (1996).
3. R. Thorneley, D. Lowe, *J. Biol. Inorg. Chem.* **1**, 576–580 (1996).
4. D. C. Rees *et al*., *Philos. Trans. Royal Soc. London Ser. A* **363**, 971–984 (2005).
5. O. Einsle, D. C. Rees, *Chem. Rev.* **120**, 4969–5004 (2020).
6. H. L. Rutledge, F. A. Tezcan, *Chem. Rev.* **120**, 5158–5193 (2020).
7. L. C. Seefeldt *et al*., *Acc. Chem. Res.* **51**, 2179–2186 (2018).
8. D. J. Lowe, R. N. Thorneley, *Biochem. J.* **224**, 877–886 (1984).
9. R. N. Thorneley, D. J. Lowe, *Biochem. J.* **224**, 887–894 (1984).
10. B. Schmid *et al*., *Biochemistry* **41**, 15557–15565 (2002).
11. F. A. Tezcan *et al*., *Science* **309**, 1377–1380 (2005).
12. T. Spatzal, K. A. Perez, O. Einsle, J. B. Howard, D. C. Rees, *Science* **345**, 1620–1623 (2014).
13. D. Sippel *et al*., *Science* **359**, 1484–1489 (2018).
14. W. Kang, C. C. Lee, A. J. Jasniewski, M. W. Ribbe, Y. Hu, *Science* **368**, 1381–1385 (2020).
15. B. M. Hoffman, D. Lukoyanov, Z.-Y. Yang, D. R. Dean, L. C. Seefeldt, *Chem. Rev.* **114**, 4041–4062 (2014).
16. L. C. Seefeldt *et al*., *Chem. Rev.* **120**, 5082–5106 (2020).
17. H. Chiu *et al*., *Biochemistry* **40**, 641–650 (2001).
18. T. A. Clarke, F. K. Yousafzai, R. R. Eady, *Biochemistry* **38**, 9906–9913 (1999).
19. G. A. Ashby, R. N. F. Thorneley, *Biochem. J.* **246**, 455–465 (1987).
20. T. A. Clarke, S. Fairhurst, D. J. Lowe, N. J. Watmough, R. R. Eady, *Biochem. J.* **39**, 201–206 (2011).
21. K. Danyal *et al*., *Proc. Natl. Acad. Sci. U.S.A.* **113**, E5783–E5791 (2016).
22. Q. Huang *et al*., *PLOS Comput. Biol.* **17**, e1008719 (2021).
23. C. P. Owens, F. E. Katz, C. H. Carter, M. A. Luca, F. A. Tezcan, *J. Am. Chem. Soc.* **137**, 12704–12712 (2015).
24. F. A. Tezcan, J. T. Kaiser, J. B. Howard, D. C. Rees, *J. Am. Chem. Soc.* **137**, 146–149 (2015).
25. H. N. Motlagh, J. O. Wrabl, J. Li, V. J. Hilser, *Nature* **508**, 331–339 (2014).
26. J. B. Howard, K. J. Kechris, D. C. Rees, A. N. Glazer, *PLOS ONE* **8**, e72751 (2013).
27. R. Y. Igarashi, L. C. Seefeldt, *Crit. Rev. Biochem. Mol. Biol.* **38**, 351–384 (2003).
28. C. N. Morrison, J. A. Hoy, L. Zhang, O. Einsle, D. C. Rees, *Biochemistry* **54**, 2052–2060 (2015).
29. C. N. Morrison, T. Spatzal, D. C. Rees, *J. Am. Chem. Soc.* **139**, 10856–10862 (2017).
30. R. R. Eady, *Chem. Rev.* **96**, 3013–3030 (1996).
31. P. A. McLean, R. A. Dixon, *Nature* **292**, 655–656 (1981).
32. M. C. Durrant, A. Francis, D. J. Lowe, W. E. Newton, K. Fisher, *Biochem. J.* **397**, 261–270 (2006).
33. C. J. Pickett, *J. Biol. Inorg. Chem.* **1**, 601–606 (1996).
34. B. Schmid *et al*., *Science* **296**, 352–356 (2002).
35. O. Einsle *et al*., *Science* **297**, 1696–1700 (2002).

ACKNOWLEDGMENTS

We thank K. Corbett, S. Narehood, J. Figueroa, and R. Subramanian for critical discussions and members of the Tezcan and Herzik labs for their assistance. Molecular graphics and analyses were performed with UCSF ChimeraX, developed by the Resource for Biocomputing, Visualization, and Informatics at the University of California, San Francisco (UCSF), with support from National Institutes of Health (NIH) grant R01-GM129325 and the Office of Cyber Infrastructure and Computational Biology, National Institute of Allergy and Infectious Diseases. We also thank members of the University of California, San Diego (UCSD)'s Cryo-EM Facility, the Stanford-Slac Cryo-EM Center (S^2C^2), and UCSD's Physics Computing Facility for help in data collection, data processing, and computational support. **Funding:** This work was supported by NIH grant R01-GM099813 (F.A.T.), NIH grant R35-GM138206 (M.A.H.), NIH grant T32-GM008326 (H.L.R. and H.P.M.N.), NASA grant 80NSSC18M0093 (F.A.T. and H.L.R., ENIGMA: Evolution of Nanomachines in Geospheres and Microbial Ancestors, NASA Astrobiology Institute Cycle 8), and the Searle Scholars Program (M.A.H.). Cryo-EM experiments were conducted at UCSD's Cryo-EM Facility as well as the Stanford-SLAC Cryo-EM Center (S^2C^2) supported by the NIH Common Fund Transformative High-Resolution Cryoelectron Microscopy program (U24 GM129541). **Author contributions:** Conceptualization: H.L.R., M.A.H., F.A.T.; Methodology: H.L.R., B.D.C., M.A.H., F.A.T.; Investigation: H.L.R., B.D.C., H.P.M.N., M.A.H., F.A.T.; Visualization: H.L.R., B.D.C., M.A.H.; Funding acquisition: M.A.H., F.A.T.; Project administration: M.A.H., F.A.T.; Supervision: M.A.H., F.A.T.; Writing – original draft: H.L.R., M.A.H., F.A.T.; Writing – review and editing: H.L.R., B.D.C., M.A.H., F.A.T. **Competing interests:** The authors declare that they have no competing interests. **Data and materials availability:** Structural models have been deposited in the Protein Data Bank with accession codes 7UT6 (^{rs}MoFeP, C_1 symmetry), 7UT7 (^{rs}MoFeP, C_2 symmetry), 7UT8 ($^{t/o}$Complex-1), 7UT9 ($^{t/o}$Complex-2), and 7UTA (BeF_x-trapped complex). The corresponding cryo-EM maps are available at the Electron Microscopy Data Bank (www.ebi.ac.uk/emdb/) with accession codes EMD-26756 (^{rs}MoFeP, C_1 symmetry), EMD-26757 (^{rs}MoFeP, C_2 symmetry), EMD-26758 ($^{t/o}$Complex-1 consensus MoFeP), EMD-26759 ($^{t/o}$Complex-1 locally refined FeP), EMD-26760 ($^{t/o}$Complex-1), EMD-26761 ($^{t/o}$Complex-2 consensus MoFeP), EMD-26762 ($^{t/o}$Complex-1 locally refined FeP), EMD-26763 ($^{t/o}$Complex-2), and EMD-26764 (BeF_x-trapped complex). All other data are available in the main text or the supplementary materials.

SUPPLEMENTARY MATERIALS

science.org/doi/10.1126/science.abq7641
Materials and Methods
Figs. S1 to S13
Tables S1 to S5
References (*36*–*51*)
MDAR Reproducibility Checklist

View/request a protocol for this paper from *Bio-protocol*.

Submitted 28 April 2022; accepted 14 July 2022
10.1126/science.abq7641